

Particle impaction efficiency and size distribution in a MSWI super heater tube bundle

Nils Erland L. Haugen^a, Steinar Kragset^{a,*}, Mette Bugge^a, Ragnar Warnecke^b, Martin Weghaus^c

^a*Sintef Energy Research, N-7465 Trondheim, Norway*

^b*GKS, Schweinfurt, Germany*

^c*Weghaus, Waldbüttelbrunn, Germany*

Abstract

Particle impaction in the super heater geometry found in the municipal solid waste incinerator (MSWI) of GKS in Schweinfurt, Germany, has been investigated. By using direct numerical simulations for the fluid flow, inertial particles coupled to the fluid through the classical Stokes' drag law have been tracked. Focus has been on the effect of flow velocity, and it is shown that decreasing the flow velocity will drastically decrease the impaction efficiency for some particle radii. Finally particle size distribution measurements are presented and used to find quantitative mass fluxes both on the front and the back side of the tubes in the super heater tube bundle.

Keywords: particle impaction, impaction efficiency, DNS, modelling, MSW, tube bundles,

1. Introduction

The deposition of particles on cylinders in an array is an important phenomenon in systems ranging from heat exchangers to fibrous filter screens. The research effort is motivated in the former class of applications by the need to minimize the total particle deposition [1–4], whereas the opposite is true for the filter systems [5–8]. A third motive

*Corresponding author

Email addresses: `nils.e.haugen@sintef.no` (Nils Erland L. Haugen), `steinar.kragset@sintef.no` (Steinar Kragset), `mette.bugge@sintef.no` (Mette Bugge), `ragnar.warnecke@gks-sw.de` (Ragnar Warnecke), `mene@weghaus.net` (Martin Weghaus)

is to reduce erosion caused by the constant bombardment of solid particles onto the cylinder surfaces in advanced coal-fired combustors and fluidised beds [9–11].

Heat exchangers in coal combustion equipments or biomass fired boilers typically consist of cylinders or tubes arranged in bundles around which the flue gas is flowing. To a various extent this gas will always contain fly ash particles resulting from impurities and inorganic material in the fuel. Ash particles in a molten or highly viscous state tend to stick to surfaces on impactation, forming deposits that cause problems in terms of corrosion, efficiency loss and high costs for maintenance. The understanding of the fluid-particle flow and the deposition mechanisms is crucial for the design of such devices [12].

The impactation of particles onto the cylinders strongly depends on the velocity field of the fluid in the vicinity of the surface. In the present study direct numerical simulations (DNS) in the sense that the Navier–Stokes equations have been solved without the use of any kind of modelling, are used in order to accurately resolve the boundary layers around the cylinders. The particle motion is described in the Lagrangian formalism, and the coupling with the fluid is through the Stokes’ drag. This enables us to study where the deposits will form and how it depends on the Reynolds and Stokes numbers. All the equations have been solved in two dimensions since basically all major flow variations are in the plane normal to the tube axes for low and intermediate Reynolds numbers. The flow is nevertheless considered a three dimensional flow, so that the simulation results can be interpreted as per unit length in the direction of the tube axes. The geometry of interest has been the super heater of the municipal solid waste incinerator (MSWI) of Gemeinschaftskraftwerk Schweinfurt GmbH (GKS) in Germany [13], from which actual measurements of the flue gas particle size distribution are presented towards the end of section 3.

In the super heater section of a boiler several impactation mechanisms might have an effect. These mechanisms are typically; inertial impactation, thermophoresis, turbulent eddy diffusion and Brownian motions. In the current work all other impactation mechanisms than inertial impactation have been neglected. The reason for doing this is twofold. Firstly inertial impactation is the most important impactation mechanism at least for large particles, and secondly inertial impactation is also the most general mechanism; by per-

forming a very fundamental study on this mechanism separately, it will be possible to clearly distinguish the importance of the different mechanisms at a later stage.

A general investigation with all the impaction mechanisms included, but under several assumptions and approximations, has been made at GKS with a commercial CFD program [14].

2. Equations

The simulations are carried out using THE PENCIL-CODE [15], where the governing fluid equations are

$$\rho \frac{D\mathbf{u}}{Dt} = -\nabla P + \nabla \cdot (2\mu \mathbf{S}) \quad (1)$$

and

$$\frac{D\rho}{Dt} = -\rho \nabla \cdot \mathbf{u}, \quad (2)$$

where t is time, P is pressure \mathbf{u} is velocity, $\mu = \rho\nu$ is the dynamic viscosity, ν is the kinematic viscosity and ρ is density.

$$\frac{D}{Dt} = \frac{\partial}{\partial t} + \mathbf{u} \cdot \nabla \quad (3)$$

is the advective derivative and the rate of strain tensor is

$$\mathbf{S} = \frac{1}{2} (\nabla \mathbf{u} + (\nabla \mathbf{u})^T) - \frac{1}{3} \nabla \cdot \mathbf{u}. \quad (4)$$

The isothermal equation of state,

$$P = c_s^2 \rho, \quad (5)$$

is used, where c_s is the speed of sound. The set of equations Eqs. (1) and (2) are solved at every grid point for every time step. As is seen in the above equations no models or filters are used. As a consequence all spatial and temporal scales must be resolved by the simulation. This requirement has led to the use of a very high resolution grid of 1024×4096 grid points in two dimensions in order to resolve a domain of 0.2 m x 0.8 m. Since no filters are used, and the discretization scheme is of high order, all the small scale kinetic energy is, as in nature, dissipated purely by the molecular viscosity.

While the fluid equations are solved at predefined grid points, the particles are tracked individually. The particle velocity is evolved in time by

$$\frac{d\mathbf{v}}{dt} = \frac{\mathbf{F}_D}{m_p}, \quad (6)$$

while the particle position behaves as

$$\frac{d\mathbf{x}}{dt} = \mathbf{v}, \quad (7)$$

where m_p , \mathbf{v} and \mathbf{x} are the mass, velocity and position of the particle, respectively. The force \mathbf{F}_D is the drag force,

$$\mathbf{F}_D = \frac{m_p}{\tau_p} (\mathbf{u} - \mathbf{v}). \quad (8)$$

No other forces are included in this work. The particle response time is

$$\tau_p = \frac{Sd^2C_c}{18\nu(1+f_c)}, \quad (9)$$

where $f_c = 0.15\text{Re}_p^{0.687}$ is negligible for small particles and $S = \rho_p/\rho$. The particle Reynolds number is $\text{Re}_p = (d|\mathbf{v} - \mathbf{u}|)/\nu$, the particle diameter is $d = 2r$ when r is the particle radius,

$$C_c = 1 + \frac{2\lambda}{d}(1.257 + 0.4e^{-(1.1d/2\lambda)}) \quad (10)$$

is the Stokes–Cunningham factor, and λ is the mean free path for a typical molecule in the gas.

Here ρ_p is the density of the particle. Assuming all particles to be small enough in order to neglect f_c and at the same time much larger than the mean free path of a molecule yields

$$\tau_p = \frac{Sd^2}{18\nu} \quad (11)$$

which is a unique number for a particular particle in a given flow. For a more detailed description of the simulations and THE PENCIL-CODE see Haugen & Kragset (2010) [16].

3. Results

The super heater of the MSWI in the GKS plant [13] consists of a non-staggered tube bundle where the center of the tubes are separated by 200 mm in the transverse direction and by 100 mm in the streamwise direction, see Figure 1. Each tube has an outer diameter of 33.7 mm and the mean velocity and temperature of the fluid approaching the super heater is 5 m/s and 600° C, respectively. This leads to a Reynolds number based on the mean velocity and the cylinder diameter of 1685 since a flue gas of 600° C yields a kinematic viscosity of approximately 10^{-4} m²/s. In all of the following we have set the particle–fluid density ratio to $S = 1000$.

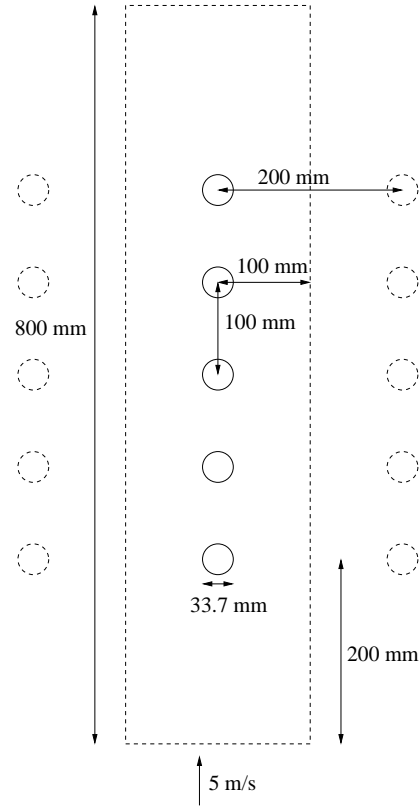


Figure 1: Here the geometry of the first five tubes of the GKS plant is shown. The dashed rectangle corresponds to the domain of the simulations, where the lower boundary is the inlet and the upper boundary is the outlet. The side boundaries are periodic, mimicking an infinite number of tube rows on each side of the domain as illustrated by the two dashed tube rows on each side of the rectangle.

The simulations presented here use periodic boundaries in the transverse direction, this means that simulating a single tube row would represent an infinite number of tube rows. This is due to the fact that for periodic boundary conditions what goes out on one side is immediately inserted on the other side of the domain. In the streamwise direction the five first tubes are simulated. Five tubes are chosen because initial calculations showed that the conditions after tube number five are essentially the same as after a tube much further downstream.

3.1. Impaction efficiency as a function of Stokes number

The main focus in the current work is the impaction efficiency $\eta = N_{\text{impact}}/N$ as a function of the Stokes and Reynolds numbers. N is here defined as the number of particles whose centers of mass initially are moving in the direction of the tube bundle and N_{impact} is the number of particles impacting on the tube. Since eddies can deflect particles substantially, particles that initially were not moving in the direction of the tube bundle may nevertheless impact, causing η to potentially exceed unity. An impaction efficiency larger than one will in certain cases result also if there is only a single target tube because of the particles' finite extents [16]: Whenever a particle whose center of mass moves closer to the tube than one particle radius, it is included into N_{impact} . In N however, all particles are regarded as point-like objects, and $N_{\text{impact}} > N$ is consequently possible.

On impact the particle is removed from the simulation. Alternatively, a rebounding of the particles could have been allowed, but to which degree this should happen would require knowledge of materials specific parameter such as the sticking coefficient. A total removal of the particles is therefore conveniently used, although the opposite extremum could equally well have been chosen. Furthermore the Stokes number is given by

$$\text{St} = \frac{\tau_p}{\tau_f} \quad (12)$$

and the Reynolds number

$$\text{Re} = \frac{uD}{\nu}, \quad (13)$$

where

$$\tau_f = \frac{D}{2u} \quad (14)$$

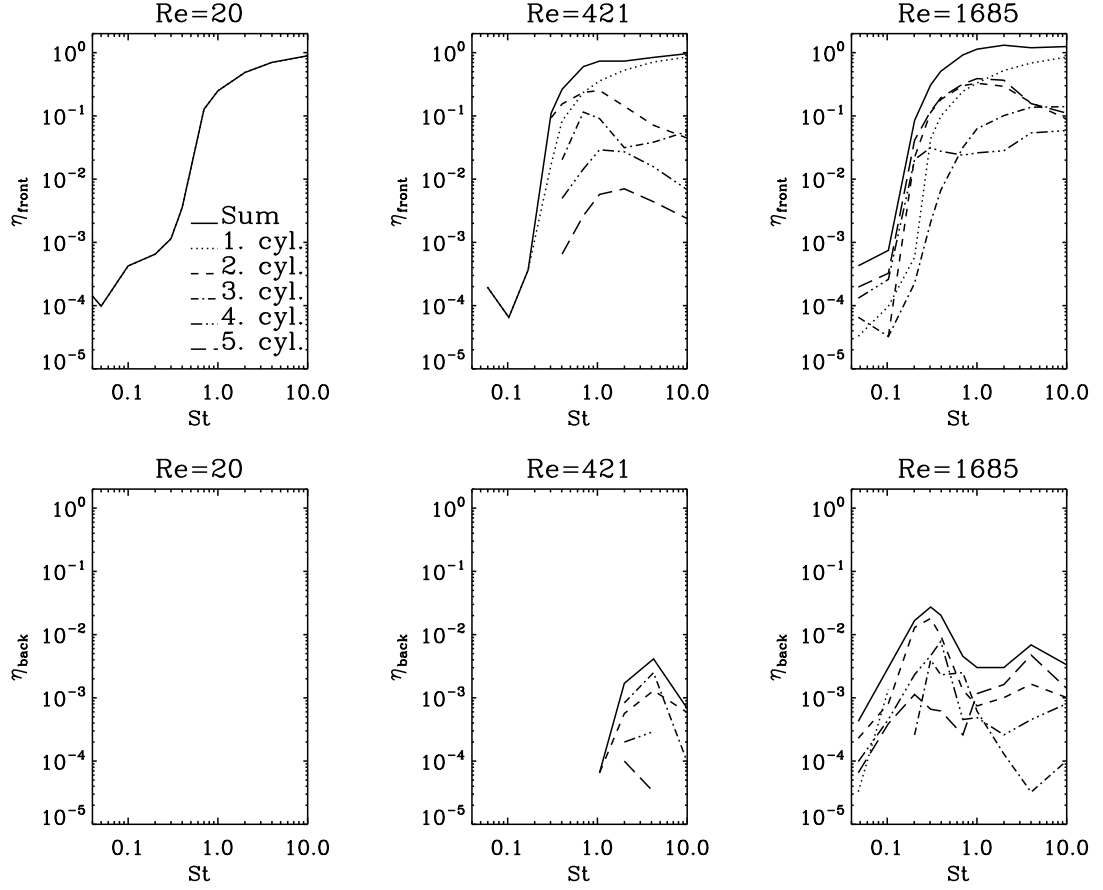


Figure 2: Front side (upper plots) and back side (lower plots) impactation efficiency as a function of Stokes number for different Reynolds numbers. Here both the impactation efficiencies for the sum of all the five tubes (solid line) and for each individual tube are shown.

is the fluid relaxation time and D is tube diameter.

In the upper row of Figure 2 the impaction efficiency on the front side of the tubes is shown as a function of Stokes number. For the low Reynolds number simulation it is seen that the only tube that experiences impaction is the first one. This is reasonable as a Reynolds number of only 20 is sub-critical to the existence of von Karman eddies, and consequently there are no fluid motion trying to force the particles towards the other cylinders as soon as they have passed the first one. Such a low Reynolds number is however not very relevant for a boiler as the heat transfer rate from the fluid to the tubes downstream of the first tube will be very low since the hot flow will pass between the tube rows without interacting with the tubes.

As the Reynolds number is increased to 421 (central upper plot in Figure 2) the presence of von Karman eddies leads to particles impacting also on the tubes downstream of the first tube. Studying the individual cylinders it can be seen that except for the initial cylinder, which has an impaction efficiency which is monotonically increasing with increasing Stokes number, all the downstream cylinders have peak impaction efficiencies in the Stokes number range of 0.7 to 2. The reason for this is that the particles with very large Stokes numbers are not as efficiently affected by the von Karman eddies, and consequently move straight on as they have passed the first tube. The particles with very small Stokes numbers do not impact on the downstream tubes simply because they follow the flow too well. The remaining are the intermediately sized particles, having the largest impaction efficiency as they are indeed affected by the von Karman eddies, but they are still large enough in order to penetrate the boundary layer around the tubes.

Increasing even further the Reynolds number to 1685 the impaction efficiency of the downstream tubes is increased even more. The major reason is the decrease in the boundary layer thickness as the Reynolds number is increased. The boundary layer is effectively working as a shield for the tubes against particle impaction. Another reason of the increased impaction efficiency is the increased intensity in the eddies generated by the cylinders. This is clearly seen in Table 1 where the rms and maximum values of the transversal velocities are shown. As expected the transversal velocities increase with Reynolds number, and the maximum velocity is even larger than the mean flow velocity for the largest Reynolds numbers. This is reflected in the observation that for $Re = 1685$

cylinders number 2, 4 and 5 all have larger impactation efficiency than the first cylinder for Stokes numbers smaller than 0.3.

Focusing now on the back side impactation it is seen in the lower left plot of Figure 2 that there is no back side impactation for $Re = 20$, this is again reasonable because there are no von Karman eddies generated for this Reynolds number and hence that there is no effect which can force the particles to move towards the back side of the cylinders.

For $Re = 421$ (central lower plot of Figure 2) it is seen that back side impactation occur for all cylinders except for the first one. The impactation efficiency is however relatively small, and it is largest around $St = 4$. In particular it is worth mentioning that the relatively large back side impactation for cylinder 3 around $St = 4$ is due to a very prominent particle stagnation between cylinder 3 and 4. Particles tend to stay in this stagnation point for long times, but as they leave they gain velocity opposite to the mean flow velocity in the direction of cylinder 3. As particles with $St = 4$ are large particles they do not have any problems penetrating the boundary layer on the back side of cylinder 3.

As the Reynolds number is increased to $Re = 1685$ (lower right plot of Figure 2) the overall back side impactation show a bimodal behavior. For the first cylinder we recover the same results as seen on a single cylinder in Haugen & Kragset (2010) [16]; that there is back side impactation only for Stokes numbers smaller than ~ 0.1 . The peak in impactation efficiencies at the smallest Stokes numbers is due to the second cylinder, while the large Stokes number peak is due to the last cylinder. It should be noted that the cause of the two peaks are fundamentally different. The peak at small Stokes numbers is caused by particles being captured in the eddies behind a given cylinder and are then given a velocity in the direction of the back side of the cylinder by this eddy. This is the same mode of back side impactation as is also found for a single cylinder [16], and it leads to impactation essentially on all angles on the back side. The second peak is caused by particles being diverted by eddies formed by cylinders further up-stream in a neighbouring tube row. These particles will then approach the cylinder not from the front side but rather from the side, which then allows for particle impactation at an angle slightly larger than 90° . It is indeed found that for Stokes numbers larger than unity almost all the impactation on the back side occurs at angles between 90° and 110° .

Table 1: Root-mean-square and maximum transversal velocities for different Reynolds numbers.

Re	$u_{\text{trans,rms}}$	$u_{\text{trans,max}}$
-	m/s	m/s
20	0.3	2.9
421	1.2	8.1
1685	1.6	11.3

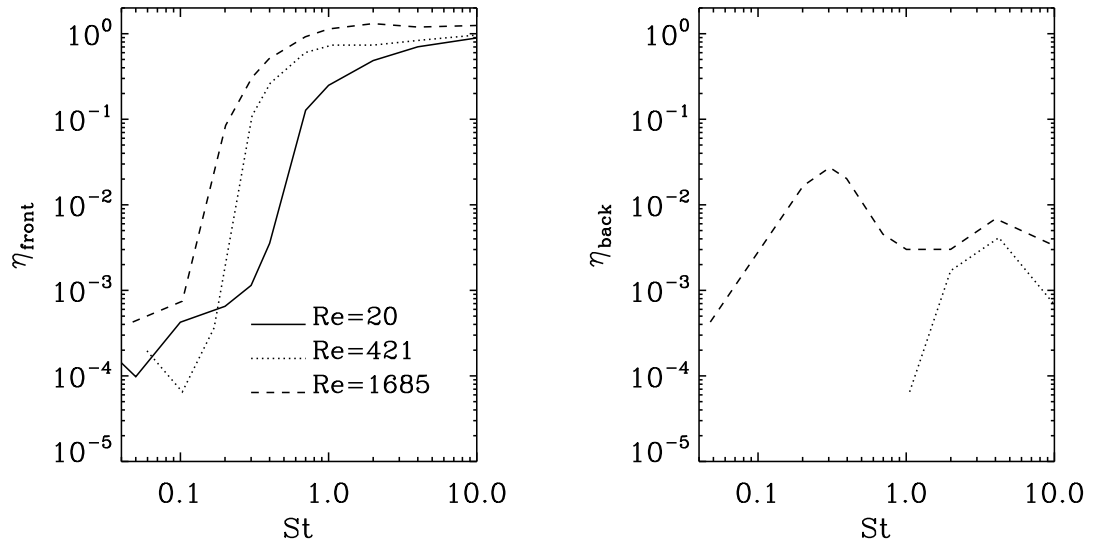


Figure 3: Front side (left plot) and back side (right plot) impactation efficiency for different Reynolds numbers as a function of the Stokes number.

In Figure 3 it is shown that the larger the Reynolds number the larger is both the total front and total back side impaction efficiency. Here total refers to the sum of the impaction efficiencies for all cylinders (which is indeed the same as the solid lines in Figure 2). In Haugen & Kragset (2010) [16] it was shown that this was also the case for the front side impaction on a single cylinder for Stokes numbers larger than ~ 0.2 . For smaller Stokes numbers, however, Haugen & Kragset (2010) [16] found that the impaction efficiency was largest for the small Reynolds numbers. Here the same trend is seen between Reynolds numbers of 20 and 421, but with a Reynolds number of 1685 the impaction efficiency is always larger than for the smaller Reynolds numbers. Regarding the back side impaction Haugen & Kragset (2010) [16] found that for a single cylinder there were no back side impaction for Stokes numbers larger than 0.13. This is clearly not the case here.

3.2. *Impaction efficiency as a function of particle diameter*

From the practical point of view, in an industrial boiler, it might be more interesting to predict the impaction efficiency as a function of the particle size than of the Stokes number. The latter is dependent on the super heater geometry and dimensions, whereas more or less the same particle size distribution will be emitted from the furnace no matter what is done with the super heater section.

The Stokes number can be expressed as a function of the Reynolds number by

$$\text{St} = \frac{d^2 Su}{9\nu D} = \frac{d^2 S}{9D^2} \text{Re} \quad (15)$$

which shows that, if the Reynolds number is decreased by either decreasing the velocity or increasing the viscosity, the Stokes number is also decreased. Consequently it is seen that the Stokes number varies linearly with the Reynolds number, such that a given particle size corresponds to a smaller Stokes number when the Reynolds number is small. From Figure 2 it is seen that the total front side impaction efficiency is monotonically decreasing with decreasing Stokes number. This means that for a given particle size the front side impaction efficiency will always decrease with the Reynolds number. This is shown more clearly in Figure 4 where the total front and back side impaction efficiency is shown as a function of particle size for the three different Reynolds numbers. It is seen that when impaction efficiency is plotted as a function of particle size the difference

between small and large Reynolds numbers is even more prominent than when plotted against Stokes number. As an example the capture efficiency of a particle with diameter of $60\text{ }\mu\text{m}$ is around 10^{-4} for $\text{Re} = 421$ while it is around 0.7 for $\text{Re} = 1685$, which is a difference by a factor of more the three orders of magnitude.

In this work the Reynolds number is changed by changing the viscosity, this is however equivalent to inversely changing the velocity.

3.3. Particle size distribution

The particle impaction efficiency has been combined with measurements of the flue gas particle size distribution in the super heater of the MSWI in Schweinfurt, Germany, in order to provide quantitative predictions for mass impaction on an actual tube bundle. In this subsection only the previously mentioned simulations with a Reynolds number of 1685 have been used.

In the measurements, the mass density $\hat{\rho}_p$ of particles in the flue gas is size fractionated using different techniques for coarse ($d \gtrsim 20\mu\text{m}$) and fine ($d \lesssim 20\mu\text{m}$) particles. For details, see [17]. Note that this density is different from the internal particle density ρ_p and is defined as the mass of the particles (of a given size) per fluid volume in which they are contained. The results for different ranges of particle sizes have accordingly been split into bins. That is, in particle bin i the mean density $\hat{\rho}_{p,i}$ of particles with diameters in the range between d_i and d_{i+1} is given (see Table 2).

As the time-step of the numerical simulations scales as $\sim d^2$ for small particle diameters it is obvious that it is not practically feasible to run simulations with extremely small particle diameters. It was found that particle sizes less than a couple of micrometers would require too much computer time. There are, however, experimental results available for $\hat{\rho}_p$ down to $0.041\text{ }\mu\text{m}$, but they have been omitted due to the restrictions introduced by the simulations.

The average particle diameter¹ d_i of the interval $(d_{i,\min}, d_{i,\max})$ will from now on be used as the representative diameter.

In the upper plot of Figure 5 the mean mass density is shown for particles in the range $3 \times 10^{-6}\text{ m}$ to $1.4 \times 10^{-3}\text{ m}$. Upstream of the first tube, the mean mass flux rate

¹The average diameter is not an arithmetic mean but is based on a fundamental knowledge of the measurements.

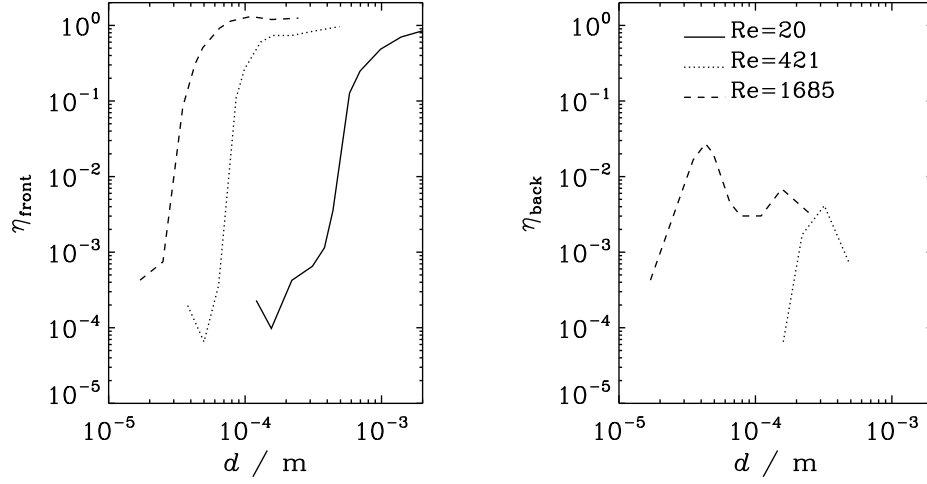


Figure 4: Front side (left plot) and back side (right plot) impactation efficiency for different Reynolds numbers as a function of the particle diameter.

Table 2: Particle size distribution just before the super heater of the MSWI in Schweinfurt, Germany

d μm	d_{\min} μm	d_{\max} μm	$\hat{\rho}_{p,i}$ g/m^3	ϕ_i $\text{g}/(\text{s m}^2)$	η_{front} -	\dot{m}_i $\text{g}/(\text{s m}^2)$
2.84	2.29	3.52	0.006	790	0.0008	0.66
4.37	3.52	5.63	0.003	263	0.0007	0.20
7.23	5.63	8.98	0.002	92	0.0006	0.05
12.0	8.98	16	0.004	65	0.0003	0.02
40	25	63	0.023	91	0.2247	21
89	63	125	0.120	315	1.1967	377
177	125	250	0.220	296	1.2082	358
354	250	500	0.270	179	1.0105	181
707	500	1000	0.078	26	1.0209	27
1400	1000	2000	0.046	7	1.0415	8

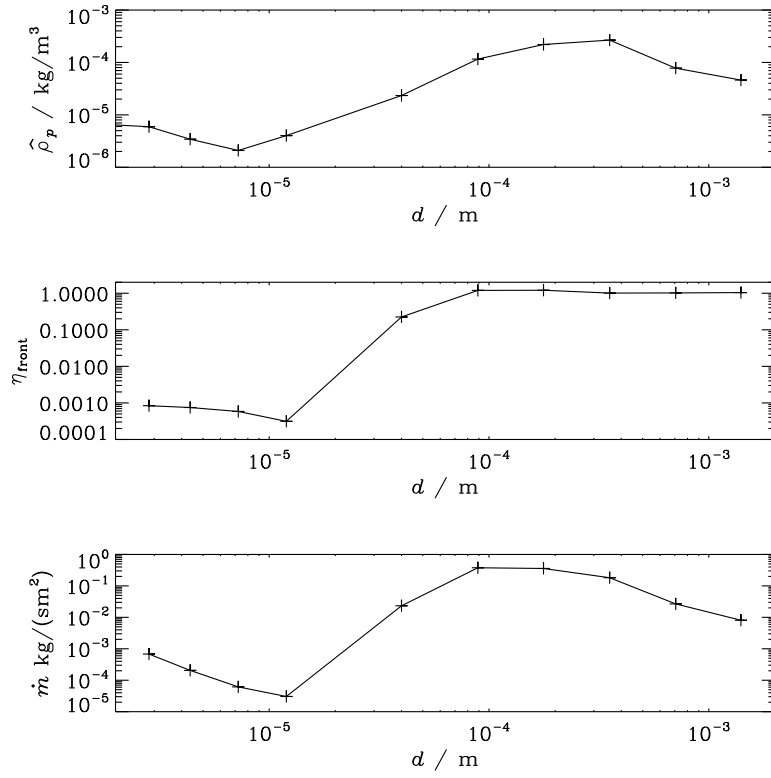


Figure 5: The upper plot show the mass density for different particle sizes, while the middle plot show the total impactation efficiency. Finally the lower plot show the specific rate of mass impactation on the front side of the tubes, per tube length, summed over all tubes in a tube row. The values result from a combination of simulation data and measurements from the MSWI in Schweinfurt, Germany.

per tube length of particles in bin i flowing in the direction of the tubes is

$$\Phi_i = \hat{\rho}_{p,i} Du, \quad (16)$$

and the corresponding specific mass flux rate for a particle diameter within the bin is then

$$\phi_i \equiv \frac{\Phi_i}{\Delta d_i} = \frac{\hat{\rho}_{p,i} Du}{\Delta d_i}, \quad (17)$$

where $\Delta d_i = d_{i+1} - d_i$. In the following all fluxes are measured per tube length.

The specific rate of mass impacting on the front side of the tubes in the tube bundle due to particles with diameters belonging to bin i is found as

$$\dot{m}_i = \phi_i \eta_{\text{front}}(d_i), \quad (18)$$

and the results are shown in the lower plot of Figure 5. In the central plot of Figure 5 the front side impaction efficiency is shown. This is essentially the same plot as the dashed line in Figure 4, but with a slightly extended range towards smaller particles.

Integrating \dot{m} over particle diameter yields the total mass captured pr. time unit. In Figure 6 \dot{m} is consequently shown in a linear fashion such that the area under the graph corresponds to the total mass impaction rate. From this it is seen that the major part of the mass deposition from particle impaction is due to particles in the range from 5×10^{-5} m to 7×10^{-3} m. So even though the impaction efficiency of all particles with $d > 7 \times 10^{-3}$ m is essentially unity, or even in excess of unity, the total impacted mass due to these particles is not very large because of their low abundance in the flow.

The specific rate of mass impacting on the *back* side of the tubes, \dot{m}_{back} , is shown in Figure 7. It is seen that the specific rate of back side mass impaction is first of all much smaller than what is found on the front side. Furthermore the main peak of \dot{m}_{back} is shifted slightly towards smaller particles compared to its front side counterpart.

4. Conclusion

In this work DNS has been used in order to accurately simulate particle impaction on a tube bundle. The tube bundle has been set up to represent the super heater in the MSWI in Schweinfurt, Germany. It is found that the particle impaction efficiency, both on the front and back side of the tubes, is very dependent on Reynolds number. This is in

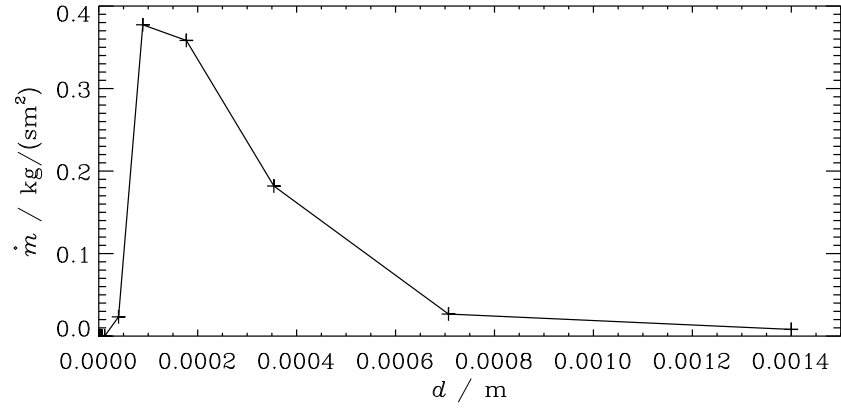


Figure 6: The total specific rate of mass impactation on the front side of all the tubes in a tube row, per tube length.

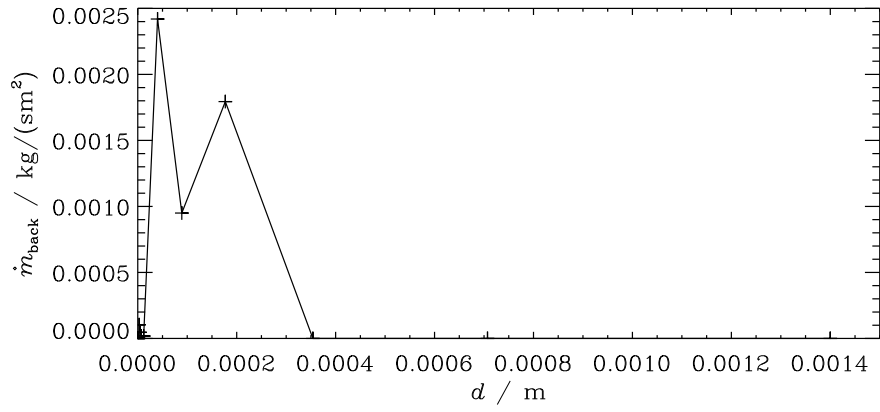


Figure 7: The total specific rate of mass impactation on the back side of all the tubes in a tube row, per tube length.

particular true for the front side capture of particles in the diameter range of 10-100 μm , where the difference between $\text{Re} = 1685$ and $\text{Re} = 421$ is of several orders of magnitude. It must be highlighted here, though, that only the drag force has been included. The inclusion of additional forces such as, Brownian motions and thermophoresis is expected to have a significant effect for small particle sizes. Allowing for the flow entering the super heater tube bundle to be turbulent may also have an effect on the results.

It is shown that the back side impaction efficiency is significantly increased for large Reynolds numbers. This is due to the increased intensity in the eddies generated by the tubes as the Reynolds number is increased.

Finally measurements of the particle size distribution found in the MSWI in Schweinfurt are presented. These measurements are then used to find quantitative results for the particle impaction rate for different particle diameters. It is found that the largest part of the mass impaction is found for particles in the range from 3×10^{-6} m to 1.4×10^{-3} m.

Acknowledgements

This work has been part of the NextGenBioWaste project, co-funded by the European Commission under the Sixth Framework Programme.

Bibliography

References

- [1] L. Y. Huang, J. S. Norman, M. Pourkashanian, A. Williams, Prediction of ash deposition on super-heater tubes from pulverized coal combustion, *Fuel* 75 (1996) 271–279.
- [2] X. Li, H. Zhou, K. Cen, Influences of various vortex structures on the dispersion and deposition of small ash particles, *Fuel* 87 (2008) 1379–1382.
- [3] D. Loehden, P. M. Walsh, A. N. Sayre, J. M. Beer, A. F. Sarofim, Generation and deposition of fly ash in the combustion of pulverised coal, *Journal of the Institute of Energy* (1989) 119–127.
- [4] S. Yilmaz, K. R. Cliffe, Particle deposition simulation using the cfd code fluent, *Journal of the Institute of Energy* (2000) 65–68.
- [5] G. Kasper, S. Schollmeier, J. Meyer, J. Hoferer, The collection efficiency of a particle-loaded single filter fiber, *Journal of Aerosol Science* 40 (12) (2009) 993 – 1009. doi:DOI:10.1016/j.jaerosci.2009.09.005. URL <http://www.sciencedirect.com/science/article/B6V6B-4XBX777-1/2/9995b5bec0f9abda0599740b04738e40>
- [6] W. Muhr, Theoretical and experimental investigation of particle deposition in fibrous filters by field and inertial forces, Dissertation, Institut für Mechanische Verfahrenstechnik und Mechanik, Universität Karlsruhe (1976).
- [7] E. Schweers, H. Umhauer, F. Löffler, Experimental investigations of particle collection on single fibres of different configurations, *Part. Part. Syst. Charact.* (1994) 275–283.
- [8] S. K. Suneja, C. H. Lee, Aerosol filtration by fibrous filters at intermediate reynolds numbers (≤ 100), *Atmospheric Environment* 8 (1974) 1081–1094.
- [9] Y. S. Morsi, J. Y. Tu, G. H. Yeoh, W. Yang, Principal characteristics of turbulent gas-particulate flow in the vicinity of single tube, *Chemical Engineering Science* 59 (15) (2004) 3141 – 3157. doi:DOI:10.1016/j.ces.2003.12.032. URL <http://www.sciencedirect.com/science/article/B6TFK-4CYNPMC-1/2/02ebd6ebfe8106ab074655f6c41258d4>

- [10] Z. Tian, J. Tu, G. Yeoh, Numerical modelling and validation of gas-particle flow in an in-line tube bank, *Computers & Chemical Engineering* 31 (9) (2007) 1064 – 1072. doi:DOI:10.1016/j.compchemeng.2006.09.008. URL <http://www.sciencedirect.com/science/article/B6TFT-4M5WHYR-2/2/6cab93d4efb386223001a98504f023fd>
- [11] J. Y. Tu, C. A. J. Fletcher, Y. S. Morsi, W. Yang, M. Behnia, Numerical and experimental studies of turbulent particle-laden gas flow in an in-line tube bank, *Chemical Engineering Science* 53 (2) (1998) 225 – 238. doi:DOI:10.1016/S0009-2509(97)00000-6. URL <http://www.sciencedirect.com/science/article/B6TFK-3SH46RH-3/2/c9bfe491bb933a9c663c66b7398f5719>
- [12] R. Scharler, J. G. M. Kuerten, K. Schulze, I. Obernberger, Numerical simulation of ash particle impaction in tube bundles a case study as a basis for a cfd based ash deposit formation model in convective heat exchangers, *VDI BERICHTE* 1988 (2007) 299–312.
- [13] GKS - Gemeinschaftskraftwerk Schweinfurt GmbH, <http://www.gks-sw.de/> (2009).
- [14] R. Warnecke, M. Weghaus, S. Horn, F. Haider, S. Maisch, V. Müller, H. Nordsieck, Entwicklung zur beschreibung der geschwindigkeit der hoch-temperatur-chlor-korrosions, in: *VDI-Wissensforum* (Hrsg.): *Feuerung und Kessel - Beläge und Korrosion in Großfeuerungsanlagen*, Düsseldorf, Germany, 2009.
- [15] THE PENCIL CODE, <http://www.nordita.org/software/pencil-code> (2009).
- [16] N. E. L. Haugen, S. Kragset, Particle impaction on a cylinder in a crossflow as function of Stokes and Reynolds number. *Journal of Fluid Mechanics*, Available on CJO 27 Jul 2010 (?) doi:10.1017/S0022112010002946
- [17] C. Deuerling, J. Maguhn, H. Nordsieck, B. Benker, R. Zimmermann, R. Warnecke, Investigation of the mechanisms of heat exchanger corrosion in a municipal waste incineration plant by analysis of the raw gas *Heat Transfer Engineering* 30 (10) (2009) 822–831. URL <http://www.informaworld.com/10.1080/01457630902751502>